

Article

Ultrasonic Assisted Sintering Using Heat Converted from Mechanical Energy

Zhiyuan Liu ¹, Yang Ge ¹, Dandan Zhao ¹, Yan Lou ¹, Yong Liu ², Yuan Wu ³, Peng Yu ⁴ and Chunyan Yu ^{5,*}

¹ Guangdong Provincial Key Laboratory of Micro/Nano Optomechatronics Engineering, College of Mechatronics and Control Engineering, Shenzhen University, Shenzhen 518060, China; zylou@szu.edu.cn (Z.L.); geyang2017@email.szu.edu.cn (Y.G.); ddzhao@szu.edu.cn (D.Z.); susanlou121@163.com (Y.L.)

² State Key Laboratory of Powder Metallurgy, Central South University, Changsha 410083, China; yonliu@csu.edu.cn

³ Beijing Advanced Innovation Center for Materials Genome Engineering, State Key Laboratory for Advanced Metals and Materials, University of Science and Technology Beijing, Beijing 100083, China; wuyuan@ustb.edu.cn

⁴ Department of Materials Science and Engineering, Southern University of Science and Technology, Shenzhen 518055, China; yup@sustech.edu.cn

⁵ College of Physics and Optoelectronic Engineering, Shenzhen University, Shenzhen 518060, China

* Correspondence: yuchunyan@szu.edu.cn

Received: 15 June 2020; Accepted: 15 July 2020; Published: 18 July 2020



Abstract: A new sintering method, namely ultrasonic assisted sintering (UAS), has been proposed using mechanical heat converted from high frequency motion between particles. Pure aluminum specimens with diameter of 5 mm and thickness of ~2 mm have been successfully sintered in two seconds. Based on the thermodynamic analysis, the underlying heating mechanism is quantitatively interpreted, which involves high-frequency interparticle friction and plastic deformation driven by ultrasonic squeezing. Consequently, temperature rises rapidly at a speed of about 300 K/s, and the maximum temperature reaches up to 0.9 times of melting point of the aluminum during UAS. The sintered specimens have a high density of dislocations, under the combined effects of dislocations and undulating stress field, volume diffusion coefficient for sintering increases by several orders of magnitude, therefore, rapid densification can be accomplished in seconds. In addition, the sintered aluminum has ultrahigh nanohardness (~1.13 GPa), which can be attributed to the hierarchical structure formed during UAS process.

Keywords: ultrasonic assisted sintering; high-frequency friction; high-frequency plastic deformation; rapid densification

1. Introduction

Sintering is one of the most economic and widely used technologies to fuse particles into bulk form. Over the past decades, the quest for a more efficient sintering process has lent lots of impetus to the development of new sintering methods [1,2]. Pressure assisted sintering, such as hot pressing and hot isostatic pressing, enables processing temperatures at level of about 200–400 degrees Celsius lower than conventional pressureless thermal sintering, and sintering time can be reduced to several hours under the assistance of pressure [3,4]. Field assisted sintering technology (FAST) mainly utilizes interparticle joule heating as internal heat source, take the representative spark plasma sintering (SPS) for example, it exhibits a high heating rate to the order of ~1000 K/min. As a result, densification rate is greatly accelerated, and sintering time is dramatically reduced to several minutes [5–7]. However,

sintering at high temperatures even lasting for minutes could lead to severe grain coarsening, and lose the benefits of initial fine microstructure before sintering [8,9]. Therefore, great efforts are continuously devoted to the development of faster sintering methods.

Friction occurs whenever two solid bodies slide against each other, mechanical work is applied against the friction. As a result, partial of the mechanical work are dissipated in the form of friction heat [10]. To utilize the frictional heat, sliding speed and frequency need to be increased to improve efficiency of local energy supply. Ultrasonic vibration is the vibration beyond those audible to human ear, that is, at frequency greater than 20 kHz [11], under such high frequency, heat can build up readily [12]. Hence, many ultrasonic vibration relevant technologies have been developed and applied in various industrial processes, such as ultrasonic machining, ultrasonic welding, and ultrasonic forming [13,14]. During the processing, high-frequency vibration could drive the adjacent components to rub against each other, friction of the contacting surfaces raise the temperature of the sliding bodies, which facilitate the mechncial processing [15–18].

Recently, ultrasonic vibration has been introduced into powder consolidation, known as ultrasonic powder consolidation or ultrasonic powder compaction. These techniques are primarily based on vibratory repacking of powder to produce green compacts with low relative density at a level of about 80~90% [19,20] and need external assisted heat for further densification sintering, no interparticale fusing was involved during the ultrasonic consolidation process [21–23]. Aluminum alloy has relative low melting point therefore needs relative small amount of energy to sinter. However, the presence of stable Al_2O_3 layer on the aluminum powder is an adverse factor affecting the sintering process, which makes aluminum difficult to sinter [24,25]. To fully exploit the frictioanl energy, a novel sintering method—ultrasonic assisted sintering (UAS)—has been developed in this study. Using pure alumium particles, the underlying sintering mechanism has been quantitatively illuminated. The aluminum can be sintered in two seconds employing the friction heat under the assistance of local plastic deformation, and a high density of dislocations is retained and hierarchical structure is formed. As a result, the obtained aluminum sample has much higher hardness compared with coventional aluminum.

2. Materials and Methods

Ultrasonic assisted sintering was performed using a specially modified ultrasonic welder (Branson 2000X, Branson ultrasonic, St. Louis, MO, USA), which was equipped with a large-powder execution device 4000 W and high resolution recording system ($\sim 2.5 \mu\text{m}$ in displacement and $\sim 1 \text{ ms}$ in time). During the sintering process, force and displacement were recorded by S-beam load cell and encoder integrated in the equipment. As shown in Figure 1, low frequency electricity (60 Hz) was converted to high frequency electricity (20 kHz) by power supply. Through a piezoelectric transducer, the high frequency electricity was transformed into ultrasonic vibration. Then, the vibration amplitude was improved by a booster. And, the high frequency vibration was delivered by punch to the aluminum powder filled in the cylindrical cavity of the mold. Load was applied by a pneumatic cylinder mounted on the top of the ultrasonic device. Four levels of pneumatic cylinder pressures: 300, 400, 500, 600 kPa were selected, sintering time were set as 2 s to ensure fully loading. During sintering, temperature rise was measured using a thermocouple embedded in the bottom of the powder.

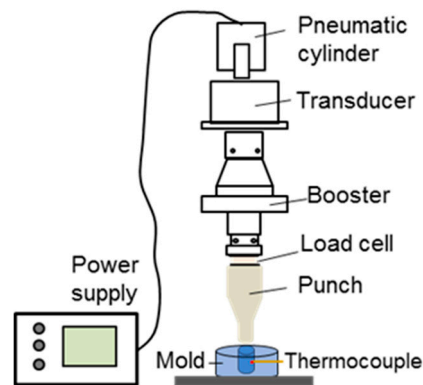


Figure 1. Schematic diagram of the ultrasonic assisted sintering (UAS) apparatus.

Gas atomized pure aluminum powder with commercial purity was used for the sintering test. Morphology of the powder was observed using scanning electron microscope (SEM ZEISS SUPRA 55, Carl Zeiss AG, Germany). Based on the Archimedes principle, densities of the sintered aluminum were measured, at least three tests were performed for each sintering parameter, relative density was calculated with reference to the theoretical density of cast aluminum $\rho_{th} = 2.7 \text{ g/cm}^3$ [26]. Structure of the sintering specimen was detected using X-ray diffractometer (Rigaku Ultima IV, Rigaku, Japan). Microstructure was observed using SEM equipment after surface polishing and electrolytic etching, and fine structure was characterized by a transmission electron microscope (TEM JEM-3200FS, JEOL, Japan) equipped with a 300 kV field emission gun. To explore the mechanical properties, nanoindentations were conducted using a nanoindenter (Hysitron TI 950, Hysitron, United States). At least 10 indent tests were performed for each specimen, the conventional aluminum provided by Hysitron company was selected as the standard sample for hardness comparison.

3. Results and Discussion

3.1. Ultrasonic Assisted Sintering Process

Figure 2a presents morphology of the gas-atomized pure aluminum particles, most of the particles have spherical shape, and some satellite particles with small tail can be found. Diameter of the particles are measured, which are ranging from 2 to 80 μm , then the average diameter is calculated to be $\sim 8 \mu\text{m}$. Figure 2b displays a typical bulk aluminum specimen sintered at pneumatic pressure of 600 kPa, the specimen has diameter of 5 mm and thickness of $\sim 2 \text{ mm}$, the shiny polished surface implies high densification capability of the newly developed UAS method.

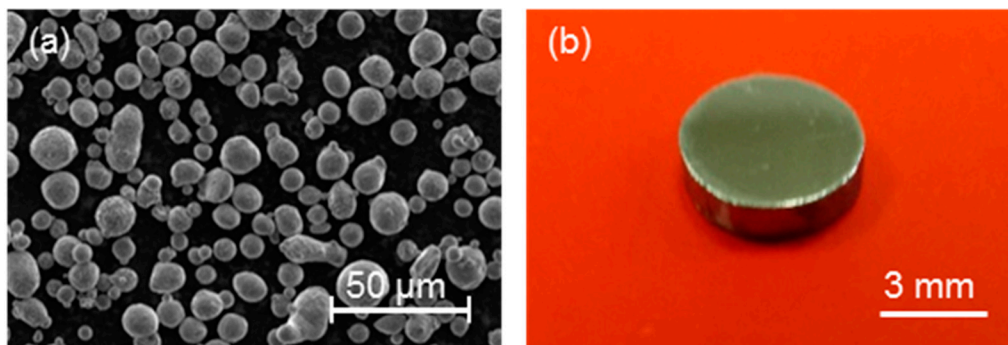


Figure 2. (a) Morphology of the original aluminum powder. (b) Bulk aluminum specimen sintered by UAS under pneumatic pressure of 600 kPa.

The aluminum particles were filled into the mold with height of 6 mm, load was applied by the pneumatic cylinder. Figure 3a shows the load–time curves during UAS process, the load increases gradually over time until a flat stage with full load achieved. As expected, the full load increases with the preset pneumatic pressure. To be specific, the full load increases from 952 to 1855 N when the pressure increase from 300 to 600 kPa. Based on the extracted full load, nominal stress applied on the particles can be calculated using equation $\sigma_n = F/A$, here F is the full load, A is cross-section area of the punch. The calculated nominal stress ranges from 48 to 94 MPa (see Table 1), relatively higher than that normally used in field assisted sintering [7]. Figure 3b presents resultant shrinkage curves of the aluminum samples during sintering, different from load–time curves, there are several fluctuations during shrinkage. For example, under pneumatic pressure of 600 kPa, after the initial loose particles repacking stage driven by the gradually increasing load, a significant shrinkage step, start from about 1.1 s, can be observed. Careful observation reveals another small shrinkage step that occurs at about 1.4 s. The shrinkage steps indicate that certain internal events can expedite the shrinkage rate in the later stage of sintering. Under smaller pressure, the shrinkage fluctuations are less distinct, suggesting that the densification is a stress dependent process during UAS.

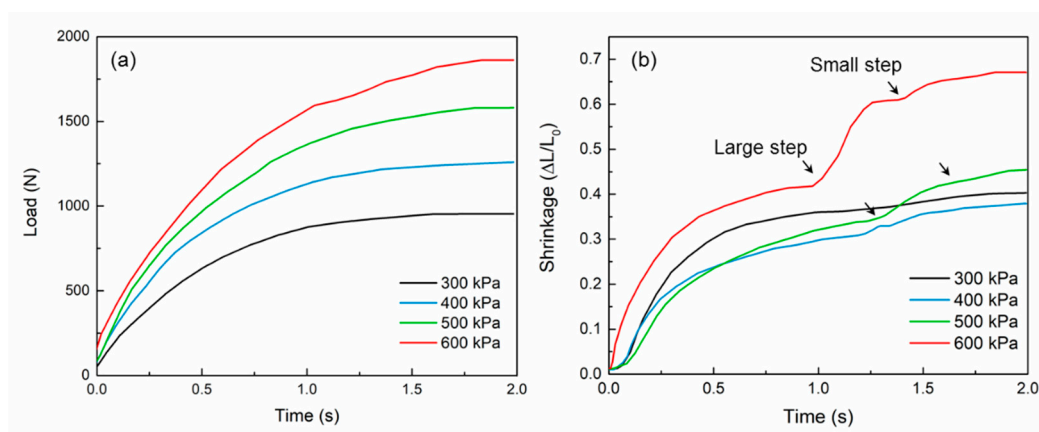


Figure 3. (a) Load–time curves during UAS process of aluminum particles. (b) Shrinkage curve during UAS process.

Table 1. Full load, nominal stress, density and temperature of the ultrasonic assisted sintering process.

Pneumatic Pressure (kPa)	Full Load (N)	Nominal Stress (MPa)	Density (g/cm ³)	Relative Density (%)	Temperature (°C)
300	952	48	2.59 ± 0.03	96.0	223
400	1254	64	2.61 ± 0.03	96.5	276
500	1575	80	2.63 ± 0.06	97.6	379
600	1855	94	2.69 ± 0.01	99.6	621

As shown in Figure 4a, density of the sintered aluminum increases with the pneumatic pressure from 2.59 to 2.69 g/cm³, attaining 99.6% of the theoretical density, that is, near-full-density sample can be obtained by UAS. It demonstrates a remarkable sintering ability of the UAS method. To explore the underlying mechanism, temperatures were in-situ measured during sintering process (see Supplementary Figure S1). The maximum temperatures are extracted and shown in Figure 4b, telling that significant temperature rise takes place during the ultrasonic compaction process. The maximum temperature T increases with the preset pneumatic pressure, specifically, T increase from 223 to 621 °C, reaching up to 0.9 times of melting temperature T_m ($T_m = 660$ °C) of the pure aluminum, which provides a basic thermodynamic requirement for the sintering. It is worth mentioning that temperature rise can also be supported by the extruded strips near the ultrasonic punch during sintering (as shown in Figure S2 of Supplementary Materials).

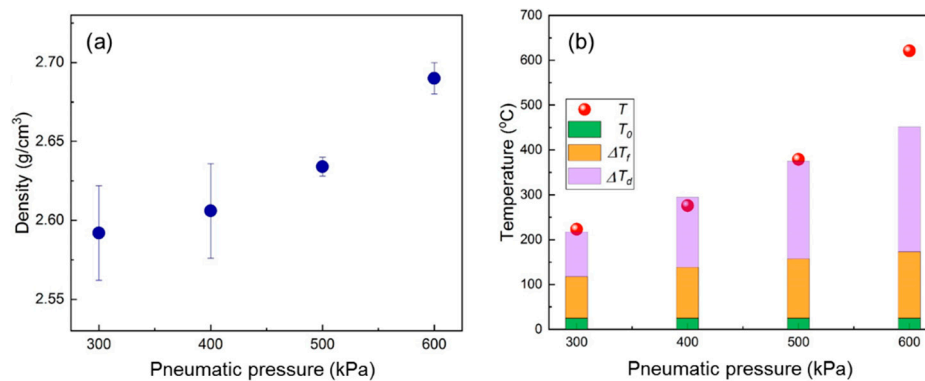


Figure 4. (a) Density of the sintered aluminum specimens using UAS method. (b) Experimental measured maximum temperature T during ultrasonic sintering. Theoretical calculated temperature rise caused by interparticle friction ΔT_f and plastic deformation ΔT_d are also presented for comparison.

3.2. Structure of the Sintered Specimens

Figure 5a shows the X-ray diffraction (XRD) curves of the sintered aluminum specimens, where typical diffraction peaks of face-centered cubic (FCC) structure can be observed. Closer examination reveals decrease of the diffraction intensity and broaden of the peaks with the increase of the sintering pressure, the reason might lay in the introduction of lattice strain under the applied high pressure during UAS, which can be approximated by Cauchy and Gaussian functions [27]

$$\frac{(\delta 2\theta)^2}{\tan^2\theta} = \frac{\lambda}{d} \left(\frac{\delta 2\theta}{\tan\theta \sin\theta} \right) + 2\langle e^2 \rangle \quad (1)$$

where $\delta 2\theta$ is the measured integral breadth of diffraction peak, θ is the peak maximum position, λ is the wave length, d is the average crystallite size, and e is the lattice strain. Furthermore, the lattice strain is related with the dislocation density ρ through equation: $\rho = 2\sqrt{3}\langle e^2 \rangle / (d \times b)$, here b is the Burgers vector (2.86×10^{-10} m for Al). It can be found that the dislocation density increases from $0.44 \times 10^{14} \text{ m}^{-2}$ to $2.54 \times 10^{14} \text{ m}^{-2}$ with the increase of applied pneumatic pressure (see Figure 5b), the value is in the same order as that of aluminum sample obtained by severe plastic deformation 3.64×10^{14} [28], indicating severe plastic deformation has been involved during the UAS process, it is also supported by the following microstructural observation results.

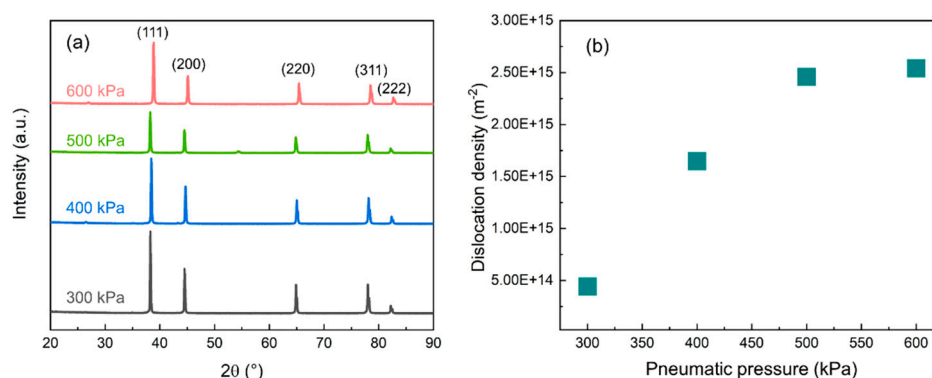


Figure 5. (a) XRD patterns of the sintered aluminum specimens. (b) Dislocation density of sintered specimens extracted from the XRD diffraction peaks.

Figure 6a shows the typical SEM microstructure of the sintered aluminum specimen after etching, clear sintering trace can be easily identified as interparticle interface. Some debris can be found located in the interface region, which is caused by the break of oxide layer during high frequency

friction [29]. Figure 6b displays high resolution TEM image of the sintered aluminum, it is found that metallurgical bond forms between adjacent particles, and a lot of dislocations are located near the interface. A closer observation reveals that high-density dislocations entangle with each other, leading to the formation of dislocation forest, wall, and cell structures [30], in agreement with the above XRD results. Furthermore, many dislocations are emitted from stress concentration sites located at interface where surface curvature changes direction, it suggests stress concentration plays an important role during UAS process. In addition, it is found that the dislocation cell has a flattened shape with thickness of ~700 nm, therefore, hierarchical structure with internal microscale grains surrounded by outer nanoscale dislocation cells is formed in the UASed aluminum specimens.

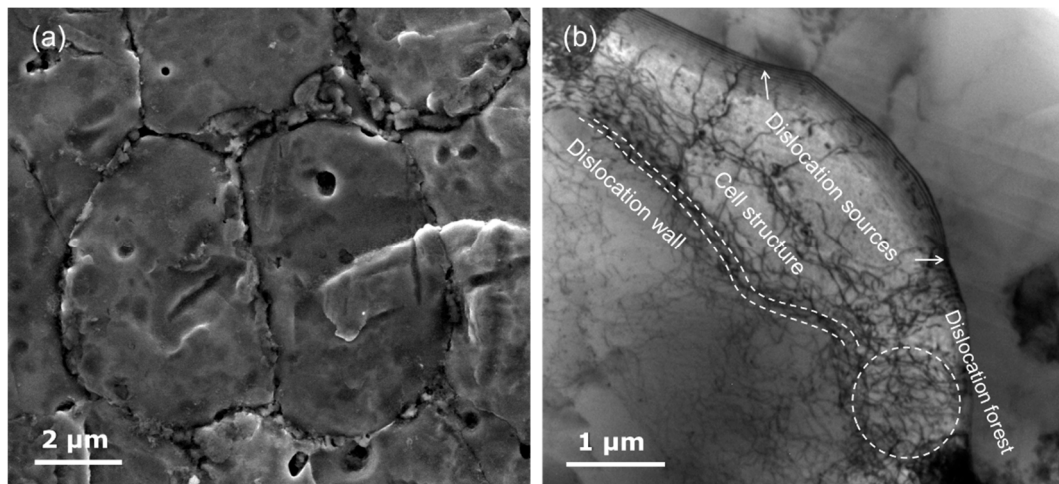


Figure 6. (a) Typical microstructure of the aluminum specimen sintered by UAS. (b) TEM image of the aluminum specimen with high density of dislocations.

3.3. Mechanism of Ultrasonic Assisted Sintering

In the initial sintering stage after particle repacking, the ultrasonic-vibration punch pushes the aluminum particles to rub against each other with high frequency in relatively small space, therefore temperature rise will take place, consistent with our previous paper [18]. Besides, it is well known that pure aluminum has a relatively low yielding stress at about 140 MPa, which is close to the applied maximum nominal pressure 90 MPa during UAS process. Furthermore, due to small contact area between spherical particles, much higher contact stress could be met in the interparticle region for the aluminum. Therefore, local plastic deformation is inevitable involved during UAS [31], which is also confirmed by the high density dislocations in Figure 6b. In addition, ultrasonic vibration exerted by the punch drives the particles to squeeze against each other with ultrasonic frequency, leading to plastic deformation occurs at high speed; therefore, most plastic deformation energy can be converted into heat [32]. Consequently, temperature rise during ultrasonic sintering is the synergy result of interfacial friction and local plastic deformation, this can be expressed by a simple relation:

$$T = T_0 + \Delta T_f + \Delta T_d \quad (2)$$

where T_0 , ΔT_f , and ΔT_d are the room temperature, temperature rise caused by friction, and plastic deformation, respectively.

Frictional heating is concentrated in the real contact area between two bodies in relative motion, based on the tribology theory, the problem can be treated as moving heat source on stationary body [33], temperature rise caused by friction can be calculated using following equation.

$$\Delta T_f = \frac{2qa}{\kappa \sqrt{\pi(1.273 + P_e)}} \quad (3)$$

where q is the rate of heat generated per unit area, $q = \mu v \sigma_c$; μ is the coefficient of friction, $\mu = 1.3$ for pure aluminum [34]; $v = A_{vib}/t_0$ is the relative friction speed, calculated to be 3 m/s; A_{vib} is the vibration amplitude at about 75 μm ; t_0 is half period of the ultrasonic vibration (2.5×10^{-5} s), a is the contact diameter (at nanoscale), κ is the thermal conductivity taken as 237 W/m·K [35]; Pe is Peclet number, expressed as $Pe = va/2k$, k is thermal diffusivity ($0.95 \text{ cm}^2/\text{s}$), the Pe values are at order of 0.001 for different pressures. The calculated ΔT_f is 95 °C under the pneumatic pressure 300 kPa, and gradually increases to 148 °C under 600 kPa, as shown in Figure 4b. These theoretical frictional temperature rises are smaller than that obtained during Ti-based amorphous powder consolidation [18], because aluminum has much larger thermal conductivity compared with Ti-based amorphous alloy (6.7 W/m·K), interparticle frictional heat can be more easily transferred to the internal body of the particles, reducing the heat concentration at interface region.

For the heat induced by high speed plastic deformation, temperature rise can be written as:

$$\Delta T_d = \frac{\beta}{\rho c} \int_0^\epsilon \sigma d\epsilon \quad (4)$$

where β is the thermal conversion efficiency of the mechanical energy (take as $\beta = 0.8$), σ is the applied stress, which can be taken as normal stress, ϵ is the vibrational strain, given by h_c/d , h_c is the contact depth variation and d is the average diameter of the particle, ρ is density, and c is specific heat (921 J/kg·K) of aluminum [35]. Based on Equation (4), ΔT_d are calculated to be ranging from 101 to 274 °C.

The sums of the theoretical calculated temperature rises are shown in Figure 4b for comparison, it can be found that the theoretical calculation agree well with the experimental data, verifying the above theoretical analysis. Note that the temperature gap at a high pneumatic pressure of 600 kPa might be caused by intense work hardening during later stages of plastic deformation, which has not been taken into consideration by the simple model. On the basis of above analyses, one can find that the mechanical ultrasonic vibration under pressure is the determinant factor contribute to the internal heating during the UAS process, which provides the driving force for the ultrafast friction and plastic deformation, and allows rapid heat accumulation in the interparticle contact zone during sintering. As a result, sintering can be accomplished in such short period of time.

Shrinkage rate curves of the UAS process are shown in Figure 7. In the early stage of sintering, a sharp downward trend can be observed, indicating that shrinkage rate decreases greatly with the increase of density. Thereafter, several rate rebounds appear in the curves, which echo shrinkage displacement steps in Figure 3b. The larger the applied pneumatic pressure, the higher the intensity of rebound. Combined with previous theoretical analysis, the UAS process can be divided into three stages—I. particle rearranging, II. interparticle heating, III. final densification—as schematically shown in the inset of Figure 7. In the first sintering stage, because the particles are loosely filled in the die cavity at the beginning, there are plenty of room for the punch to move downward through particle rearranging, therefore the shrinkage rate is high. With the increase of applied pressure, aluminum particles gradually rearrange to denser state, thus the shrinkage rate decreases. To a certain state, the particles need to squeeze against each other to rearrange further. Driven by the ultrasonic vibration, high speed interparticle sliding takes place, frictional heating begins and reduces the resistance of densification, manifested as the first shrinkage rate rebound [18]. When a more densely packed state is arrived at without sliding space left between particles, the shrinkage rate drops once again. With further increase of cylinder pressure, local contact stress between particles will climb to the yielding point of aluminum. Under the vibrational stress, high-speed plastic deformation engenders further heating up and therefore improves the densification rate, represented as the second shrinkage rate rebound. In the final densification stage, with an increase of interparticle contact area, the local contact stress decreases gradually. As a result, mechanical heating stops working and the densification process slows down in the end. Overall, the excellent agreement between the shrinkage rate curves, morphologies of sintered specimen, and theoretical analysis confirms that the sintering mechanism of

UAS can be attributed to the mechanical friction assisted by plastic deformation at ultrasonic frequency, and the whole sintering can be divided into three stages roughly.

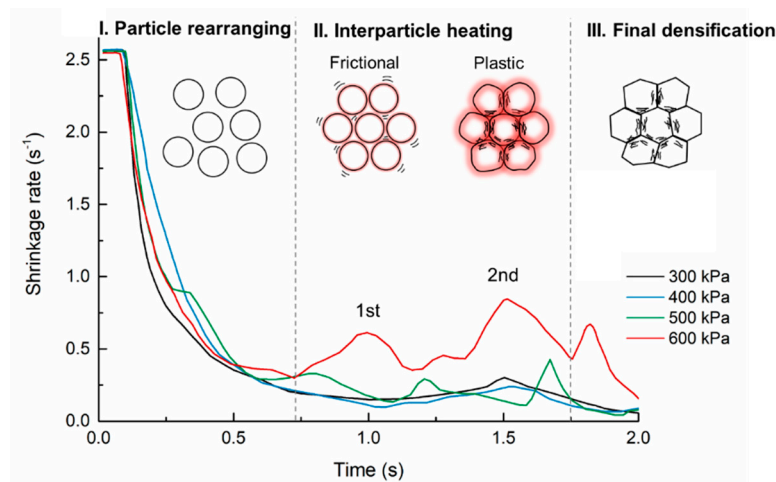


Figure 7. Shrinkage rate curves during UAS process. The inset is schematic drawing of the densification process, which including three stages: I. Particle rearranging; II. Interparticle heating; III. Final densification.

3.4. Hardness of the Sintered Aluminum Specimens

To explore mechanical properties of the sintered aluminum specimens, nanoindentation tests were performed. Force–depth curves are shown in Figure 8a with standard aluminum also presented for comparison, it can be found that the sintered specimens have much smaller penetration depth compared with standard aluminum under the same force 8000 μN , and the depth decreases with increase of sintering pressure. Using Oliver-Pharr approach [36], hardness data is extracted and shown in Figure 8b, increases from 0.90 to 1.13 GPa, which is much larger than standard aluminum (~ 0.4 GPa) [37]. It is known that hardness correlates linearly with strength [38], as expressed by equation $H = 3\sigma$. The estimated yielding strength of the UASed pure aluminum reaches up to ~ 300 – 380 MPa, close to yielding strength of AA2xxx-series aluminum alloy. Such high strength might be caused by the hierarchical structure—i.e., microscale grains surrounded by nano dislocation cells—obtained during the UAS process (Figure 6b), which has better efficiency to impede dislocation motion and results in higher strength. In addition, the thickness of the aluminum oxide layer presented on the surface of original particles is about tens of nanometers [24], volume fraction can be estimated to be $\sim 2\%$. Due to the short processing time, volume fraction changes little during UAS, therefore its effect on hardness is negligible [39]. In-depth explanation for the high hardness needs further symmetrical investigation.

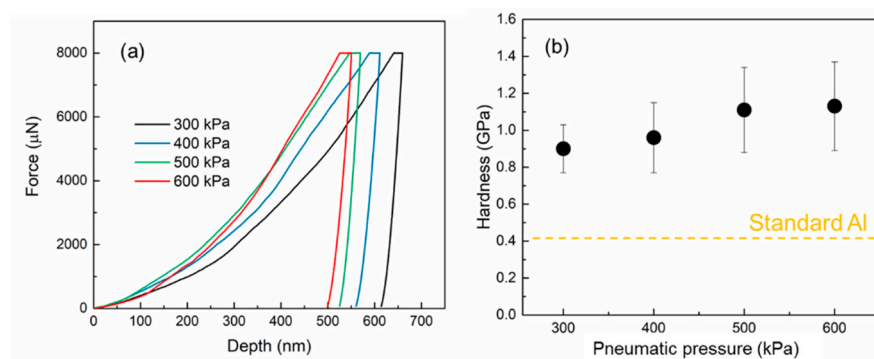


Figure 8. (a) Nanoindentation force–depth curves of the sintered and conventional aluminum specimens. (b) Hardness value of the aluminum specimens.

Before closing, it is worth mentioning that many FAST variants have recently been developed to improve efficiency of sintering further, such as medium-frequency electrical resistance sintering (MF-ERS), it uses medium frequency electric current to achieve sintering within one second [40–42]. Compare with the MF-ERS method, UAS utilizes the mechanical energy as heat source; broadly, there are three similarities between UAS and MF-ERS: (1) Short processing time in one or two seconds. (2) Low processing pressures around 100 MPa with assistance of ultrasonic friction or medium-frequency electrical energy to achieve very high densities. (3) Possibility of operating in the air. However, UAS merges the consolidation and sintering into a single step, which need no pre-compaction. High density of dislocations accumulated during plastic deformation are retained after sintering caused by the short processing time and localized contact of the adjacent particles during UAS. As a result, the hardnesses of UASed aluminum specimens are much larger. These further emphasize the great significance of the newly developed UAS method. Due to internal interparticle heating, the maximum heating rate can attain ~300 K/s, which is one order of magnitude higher than that of spark plasma sintering [43]. Such high heating rate provides the basic thermodynamic requirement for fast sintering. In addition, during the high-frequency plastic deformation, numerous dislocations are generated underneath the contact zone, and lots of vacancies are created by motion of dislocation kinks, which further reduces the activation energy of diffusion by more than half. As a result, diffusion coefficient can be increased by several orders of magnitude [44,45]. Besides, it is reported that volume diffusion can be further accelerated by the ultrasonic force field [46,47]. The much larger diffusion coefficient offers kinetic requirement for fast sintering. Consequently, rapid densification can be achieved in seconds during UAS. Furthermore, fine structure of the original particle can be maintained during this fast sintering process, and severe plastic deformation are introduced, leading to further grain refinement [48]; therefore, UAS provides a new approach to fabricate materials with hierarchical structure and better mechanical performance.

4. Conclusions

In summary, using mechanical energy, a novel ultrasonic assisted sintering (UAS) method has been proposed, and near-full-density pure aluminum specimens have been successfully sintered in 2 s. The rapid heating effect is caused by internal thermal energy converted from high-frequency interparticle friction and plastic deformation driven by the ultrasonic punch, and the underlying sintering mechanism is quantitatively interpreted accordingly. The densification process of UAS can be divided into three stages—I. Particle rearranging, II. Interparticle heating, III. Final densification. In addition, the sintered aluminum specimens have ultrahigh hardnesses due to the hierarchical structure formed during sintering.

Supplementary Materials: The following are available online at <http://www.mdpi.com/2075-4701/10/7/971/s1>, Figure S1: Temperature rise during ultrasonic assisted sintering process, Figure S2: The snapshots showing aluminum strips squeezed out from the gap between punch and mold during ultrasonic assisted sintering.

Author Contributions: Conceptualization, Z.L. and C.Y.; methodology, Y.G.; validation, Y.L. (Yong Liu) and P.Y.; Formal analysis, Y.L. (Yan Lou); investigation, D.Z.; writing—original draft preparation, Y.G.; writing—review and editing, C.Y.; visualization, Y.W.; supervision, Z.L. All authors have read and agreed to the published version of the manuscript.

Funding: The authors would like to acknowledge the financial support of National Natural Science Foundation of China (Grant Nos. 51971149, 51701125), and acknowledge the funding from Science and Technology Innovation Commission of Shenzhen (no. KQJSCX20180328095612712).

Acknowledgments: The authors want to acknowledge the assistance on HRTEM observation received from the Electron Microscope Center of the Shenzhen University.

Conflicts of Interest: The authors declare no conflict of interest, and the funders had no role in the design of the study; in the collection, analyses, or interpretation of data; in the writing of the manuscript, or in the decision to publish the results.

References

1. Huang, K.; Yang, Y.; Qin, Y.; Yang, G.; Yin, D. A new densification mechanism of copper powder sintered under an electrical field. *Scr. Mater.* **2015**, *99*, 85–88. [[CrossRef](#)]
2. Fang, Z.Z.; Wang, X.; Ryu, T.; Hwang, K.S.; Sohn, H.Y. Synthesis, sintering, and mechanical properties of nanocrystalline cemented tungsten carbide—A review. *Int. J. Refract. Met. Hard Mater.* **2009**, *27*, 288–299. [[CrossRef](#)]
3. Senkov, O.N.; Scott, J.M.; Senkova, S.V.; Miracle, D.B.; Woodward, C.F. Microstructure and room temperature properties of a high-entropy TaNbHfZrTi alloy. *J. Alloys Compd.* **2011**, *509*, 6043–6048. [[CrossRef](#)]
4. Atkinson, H.V.; Davies, S. Fundamental aspects of hot isostatic pressing: An overview. *Met. Mater. Trans. A* **2000**, *31*, 2981–3000. [[CrossRef](#)]
5. Yu, M.; Grasso, S.; McKinnon, R.; Saunders, T.; Reece, M.J. Review of flash sintering: Materials, mechanisms and modelling. *Adv. Appl. Ceram.* **2017**, *116*, 24–60. [[CrossRef](#)]
6. Shen, Z.J.; Johnsson, M.; Zhao, Z.; Nygren, M. Spark plasma sintering of alumina. *J. Am. Ceram. Soc.* **2002**, *85*, 1921–1927. [[CrossRef](#)]
7. Mamedov, V. Spark plasma sintering as advanced PM sintering method. *Powder Met.* **2002**, *45*, 322–328. [[CrossRef](#)]
8. Park, M.; Schuh, C.A. Accelerated sintering in phase-separating nanostructured alloys. *Nat. Commun.* **2015**, *6*, 6. [[CrossRef](#)]
9. Bordia, R.K.; Kang, S.-J.L.; Olevsky, E.A. Current understanding and future research directions at the onset of the next century of sintering science and technology. *J. Am. Ceram. Soc.* **2017**, *100*, 2314–2352. [[CrossRef](#)]
10. Basu, B.; Kalin, M. Frictional heating and contact temperature. In *Tribology of Ceramics and Composites*; Wiley-American Ceramic Society: Hoboken, NJ, USA, 2011; pp. 60–69.
11. Ensminger, D.; Bond, L.J. *Ultrasonics: Fundamentals, Technologies, and Applications*; CRC Press: Boca Raton, FL, USA, 2011.
12. Lou, Y.; Liu, X.; Yang, X.; Ge, Y.; Zhao, D.; Wang, H.; Zhang, L.-C.; Liu, Z. Fast rejuvenation in bulk metallic glass induced by ultrasonic vibration precompression. *Intermetallics* **2020**, *118*, 106687. [[CrossRef](#)]
13. Thoe, T.B.; Aspinwall, D.K.; Wise, M.L.H. Review on ultrasonic machining. *Int. J. Mach. Tools Manuf.* **1998**, *38*, 239–255. [[CrossRef](#)]
14. Ma, J.; Yang, C.; Liu, X.; Shang, B.; He, Q.; Li, F.; Wang, T.; Wei, D.; Liang, X.; Wu, X.; et al. Fast surface dynamics enabled cold joining of metallic glasses. *Sci. Adv.* **2019**, *5*, eaax7256. [[CrossRef](#)]
15. Musa, M.A.; Ahmad Najmuddin Wan Saidin, W.; Kasim, N.I.; Ibrahim, M.I.; Mohamad Noor, N. A review on ultrasonic welding capability: Breakaway from traditional plastic. *Appl. Mech. Mater.* **2015**, *789*, 136–140. [[CrossRef](#)]
16. Tsujino, J. Review of ultrasonic welding of metal and plastic materials. *J. Acoust. Soc. Jpn.* **1989**, *45*, 409–415.
17. Tsujino, J.; Ueoka, T.; Hasegawa, K.; Fujita, Y.; Shiraki, T.; Okada, T.; Tamura, T. New methods of ultrasonic welding of metal and plastic materials. *Ultrasonics* **1996**, *34*, 177–185. [[CrossRef](#)]
18. Chen, P.; Liao, W.B.; Liu, L.H.; Luo, F.; Wu, X.Y.; Li, P.J.; Yang, C.; Yan, M.; Liu, Y.; Zhang, L.C.; et al. Ultrafast consolidation of bulk nanocrystalline titanium alloy through ultrasonic vibration. *Sci. Rep.* **2018**, *8*, 801. [[CrossRef](#)] [[PubMed](#)]
19. Gheybi Hashemabad, S.; Ando, T. Ignition characteristics of hybrid Al–Ni–Fe₂O₃ and Al–Ni–CuO reactive composites fabricated by ultrasonic powder consolidation. *Combust. Flame* **2015**, *162*, 1144–1152. [[CrossRef](#)]
20. Abedini, R.; Abdullah, A.; Alizadeh, Y. Ultrasonic assisted hot metal powder compaction. *Ultrason. Sonochem.* **2017**, *38*, 704–710. [[CrossRef](#)]
21. Erdeniz, D.; Ando, T. Fabrication of micro/nano structured aluminum-nickel energetic composites by means of ultrasonic powder consolidation. *Int. J. Mater. Res.* **2013**, *104*, 386–391. [[CrossRef](#)]
22. Abedini, R.; Abdullah, A.; Alizadeh, Y. Ultrasonic hot powder compaction of Ti-6Al-4V. *Ultrason. Sonochem.* **2017**, *37*, 640–647. [[CrossRef](#)]
23. Liu, Z. Densification and Metallurgical Bonding in Copper Powder Compact during Ultrasonic Powder Consolidation. Master's Thesis, Northeastern University, Boston, MA, USA, 2015.
24. Fang, Z.Z. *Sintering of Advanced Materials*; Woodhead Publishing Limited: Cambridge, UK, 2010; p. 484.
25. Schaffer, G.B.; Hall, B.J. The influence of the atmosphere on the sintering of aluminum. *Met. Mater. Trans. A* **2002**, *33*, 3279–3284. [[CrossRef](#)]

26. Awotunde, M.A.; Adegbenjo, A.O.; Obadele, B.A.; Okoro, M.; Shongwe, B.M.; Olubambi, P.A. Influence of sintering methods on the mechanical properties of aluminium nanocomposites reinforced with carbonaceous compounds: A review. *J. Mater. Res. Technol.* **2019**, *8*, 2432–2449. [[CrossRef](#)]
27. Lu, J.X.; Wu, X.Y.; Liu, Z.Y.; Chen, X.Q.; Xu, B.; Wu, Z.Z.; Ruan, S.C. Microstructure and mechanical properties of ultrafine-grained copper produced using intermittent ultrasonic-assisted equal-channel angular pressing. *Met. Mater. Trans. A* **2016**, *47*, 4648–4658. [[CrossRef](#)]
28. Miyajima, Y.; Mitsuhara, M.; Hata, S.; Nakashima, H.; Tsuji, N. Quantification of internal dislocation density using scanning transmission electron microscopy in ultrafine grained pure aluminium fabricated by severe plastic deformation. *Mater. Sci. Eng. A* **2010**, *528*, 776–779. [[CrossRef](#)]
29. Chen, W.; Liu, Z.; Schroers, J. Joining of bulk metallic glasses in air. *Acta Mater.* **2014**, *62*, 49–57. [[CrossRef](#)]
30. Madec, R.; Devincre, B.; Kubin, L.P. From dislocation junctions to forest hardening. *Phys. Rev. Lett.* **2002**, *89*, 4. [[CrossRef](#)]
31. Diouf, S.; Molinari, A. Densification mechanisms in spark plasma sintering: Effect of particle size and pressure. *Powder Technol.* **2012**, *221*, 220–227. [[CrossRef](#)]
32. Kapoor, R.; Nemat-Nasser, S. Determination of temperature rise during high strain rate deformation. *Mech. Mater.* **1998**, *27*, 1–12. [[CrossRef](#)]
33. Bhushan, B. *Modern Tribology Handbook*, 2nd ed.; CRC Press: Boca Raton, FL, USA, 2000.
34. Bhushan, B. *Introduction to Tribology*; Wiley: Columbus, OH, USA, 2013; Volume 2, p. 711.
35. Touloukian, Y.S.; Powell, R.W.; Ho, C.Y.; Klemens, P.G. *The TPRC Data Series*; Purdue Research Foundation: West Lafayette, IN, USA, 1970; Volume 1.
36. Oliver, W.C.; Pharr, G.M. An improved technique for determining hardness and elastic modulus using load and displacement sensing indentation experiments. *J. Mater. Res.* **1992**, *7*, 1564–1583. [[CrossRef](#)]
37. Aliyu, I.K.; Saheb, N.; Hassan, S.F.; Al-Aqeeli, N. Microstructure and properties of spark plasma sintered aluminum containing 1 wt.% SiC nanoparticles. *Metals* **2015**, *5*, 70–83. [[CrossRef](#)]
38. Liu, Z.Y.; Yang, Y.; Guo, S.; Liu, X.J.; Lu, J.; Liu, Y.H.; Liu, C.T. Cooling rate effect on Young's modulus and hardness of a Zr-based metallic glass. *J. Alloys Compd.* **2011**, *509*, 3269–3273. [[CrossRef](#)]
39. Nuruzzaman, D.; Kamaruzaman, F.; Azmi, N. Effect of sintering temperature on the properties of aluminium-aluminium oxide composite materials. *Int. J. Eng. Mater. Manuf.* **2016**, *1*, 59. [[CrossRef](#)]
40. Ternero, F.; Astacio, R.; Caballero, E.S.; Cuevas, F.G.; Montes, J.M. Influence of processing parameters on the conduct of electrical resistance sintering of iron powders. *Metals* **2020**, *10*, 14. [[CrossRef](#)]
41. Orrù, R.; Licheri, R.; Locci, A.M.; Cincotti, A.; Cao, G. Consolidation/synthesis of materials by electric current activated/assisted sintering. *Mater. Sci. Eng. R Rep.* **2009**, *63*, 127–287. [[CrossRef](#)]
42. Fais, A. A faster FAST: Electro-sinter-forging. *Met. Powder Rep.* **2018**, *73*, 80–86. [[CrossRef](#)]
43. Liu, L.H.; Yang, C.; Yao, Y.G.; Wang, F.; Zhang, W.W.; Long, Y.; Li, Y.Y. Densification mechanism of Ti-based metallic glass powders during spark plasma sintering process. *Intermetallics* **2015**, *66*, 1–7. [[CrossRef](#)]
44. Ruoff, A.L.; Balluffi, R.W. Strain-enhanced diffusion in metals. II. dislocation and grain-boundary short-circuiting models. *J. Appl. Phys.* **1963**, *34*, 1848–1853. [[CrossRef](#)]
45. Rozenberg, L. *Physical Principles of Ultrasonic Technology*, 1st ed.; Springer: New York, NY, USA, 1973.
46. Vasil'ev, L.S. To the theory of the anomalously high diffusion rate in metals under shock action: I. Basic equations of diffusion mass transfer upon plastic deformation of materials. *Phys. Met. Met.* **2009**, *107*, 330–340. [[CrossRef](#)]
47. Yang, J.W.; Zhang, J.; Qiao, J. Molecular dynamics simulations of atomic diffusion during the Al-Cu ultrasonic welding process. *Materials* **2019**, *12*, 11. [[CrossRef](#)]
48. Estrin, Y.; Vinogradov, A. Extreme grain refinement by severe plastic deformation: A wealth of challenging science. *Acta Mater.* **2013**, *61*, 782–817. [[CrossRef](#)]

